Universal sheet resistance and revised phase diagram of the cuprate high-temperature superconductors

Neven Barišić[a,b,c,d], Mun K. Chan[a], Yuan Li[e], Guichuan Yu[a], Xudong Zhao[a,f], Martin Dressel[b], Ana Smontara[c], and Martin Greven[a,1]

[a]School of Physics and Astronomy, University of Minnesota, Minneapolis, MN 55455; [b]1. Physikalisches Institut, Universität Stuttgart, D-70550 Stuttgart, Germany; [c]Institute of Physics, HR-10000 Zagreb, Croatia; [d]Service de Physique de l'Etat Condensé, Commissariat à l'Énergie Atomique et aux Énergies Alternatives–Direction des Sciences de la Matière–Institut Rayonnement Matière de Saclay, F-91198 Gif-sur-Yvette, France; [e]International Center for Quantum Materials, School of Physics, Peking University, Beijing 100871, China; and [f]State Key Lab of Inorganic Synthesis and Preparative Chemistry, College of Chemistry, Jilin University, Changchun 130012, China

Upon introducing charge carriers into the copper–oxygen sheets of the enigmatic lamellar cuprates, the ground state evolves from an insulator to a superconductor and eventually to a seemingly conventional metal (a Fermi liquid). Much has remained elusive about the nature of this evolution and about the peculiar metallic state at intermediate hole-carrier concentrations (p). The planar resistivity of this unconventional metal exhibits a linear temperature dependence ($\rho \propto T$) that is disrupted upon cooling toward the superconducting state by the opening of a partial gap (the pseudogap) on the Fermi surface. Here, we first demonstrate for the quintessential compound HgBa$_2$CuO$_{4+\delta}$ a dramatic switch from linear to purely quadratic (Fermi liquid-like, $\rho \propto T^2$) resistive behavior in the pseudogap regime. Despite the considerable variation in crystal structures and disorder among different compounds, our result together with prior work gives insight into the p-T phase diagram and reveals the fundamental resistance per copper–oxygen sheet in both linear ($\rho_\square = A_{1\square}T$) and quadratic ($\rho_\square = A_{2\square}T^2$) regimes, with $A_{1\square} \propto A_{2\square} \propto 1/p$. Theoretical models can now be benchmarked against this remarkably simple universal behavior. Deviations from this underlying behavior can be expected to lead to new insight into the nonuniversal features exhibited by certain compounds.

When exploring the properties of a material, the resistivity is the quantity that is often first measured, but last understood. It is an observable that corresponds to a weighted integration over the whole Fermi surface (see *SI Appendix* for details). Consequently, the resistivity is highly sensitive to changes in electronic behavior, and hence regularly used to detect phase transitions and determine phase diagrams. However, for the same reason, the resistivity typically exhibits complex temperature, magnetic field, etc., dependences. Nevertheless, when simple temperature dependences are observed, such as power law in a metal or exponential in a semiconductor, this usually provides important insight into the fundamental properties of a material (1). Only in rare cases, such as the quantum Hall effect in correlated 2D electron systems, has the magnitude of the resistivity been found to be the same for an entire class of materials (2).

In the case of the cuprates, the close proximity to the Mott insulator has long been argued to imply a purely electronic superconducting mechanism (3), yet the peculiar metallic state from which the superconductivity emerges upon cooling has remained an enigma. Part of the difficulty stems from the fact that the well over 100 cuprate superconductors exhibit nonuniversal temperature-doping phase diagrams due to significant differences in superconducting transition temperatures (T_c), crystal structures, disorder, competing phases, etc. (4).

Here, we first report quantitative planar dc resistivity results for the structurally simple single-CuO$_2$–layer compound HgBa$_2$CuO$_{4+\delta}$ (Hg1201). Above the pseudogap temperature T^* (5, 6), we observe the well-known yet poorly understood linear behavior $\rho = A_1T$. Upon further cooling, we find a distinct switch to a purely quadratic dependence, $\rho = A_2T^2$, that holds between the lower

characteristic temperature T^{**} and the measurable appearance of superconducting fluctuations at T', just above T_c ($T^* > T^{**} > T' > T_c$). We then present a systematic analysis of prior data for double-layer YBa$_2$Cu$_3$O$_{6+\delta}$ (YBCO) (7–12) as well as single-layer La$_{2-x}$Sr$_x$CuO$_4$ (LSCO) (8, 9, 13–16) and Tl$_2$Ba$_2$CuO$_{6+\delta}$ (Tl2201) (13, 17). The distinct crystal structures of these four cuprates are shown in Fig. 1. Due to the quasi-2D electronic structure of the cuprates, with its underlying square-planar CuO$_2$ sheet, it is natural to consider the resistance $\rho_\square$ per Cu–O sheet (*SI Appendix, section 3*), although this is rarely done. Our simple and entirely model-free analysis reveals that, across a large part of the phase diagram, the sheet resistance coefficients $A_{1\square}$ and $A_{2\square}$ are universal. Moreover, these coefficients are simply proportional to the inverse hole concentration: $A_{1\square} \propto A_{2\square} \propto 1/p$. Our findings give profound insight into the phase diagram and the nature of the conducting states of the high-T_c cuprates.

Results

Planar Resistivity and Characteristic Temperatures. Hg1201 crystals were prepared according to a previously reported procedure (18, 19). The in-plane dc resistivities of three underdoped samples with $T_c = 80$ K are displayed in Fig. 2A, and the magnetization characterization for one of them is shown in Fig. 2B. Regardless of their significantly different dimensions (e.g., a–b dimensions vary between about 0.01 and 1 mm), the samples exhibit identical temperature dependences (Fig. 2C), and hence a high degree of homogeneity. Extrapolation of the high-temperature linear behavior ($\rho = \rho_0 + A_1T$) to zero temperature gives $T^* \approx 280$ K and reveals a negligible residual resistivity. Such a small ρ_0 is usually taken as the signature of a very clean metallic system, with minimal extrinsic and intrinsic disorder. This is noteworthy, because the underdoped cuprates typically exhibit a large ρ_0 that increases with decreasing doping (6, 20).

The quadratic temperature dependence is demonstrated in Fig. 2D. For the $T_c = 80$ K samples, it is found below $T^{**} \approx 170$ K and spans about 80 K in temperature before the influence of superconducting fluctuations is noticeable at T'. As shown in Fig. 3 A–C, this behavior is also observed at lower doping (samples with $T_c = 47$ K and 67 K). In other cuprates, the pure underlying quadratic behavior tends to be masked: for example, we found no published evidence for Bi$_2$Sr$_2$CuO$_{6+\delta}$ (Bi2201) and Bi$_2$Sr$_2$CaCu$_2$O$_{8+\delta}$ (Bi2212), two well-studied compounds for

PHYSICS
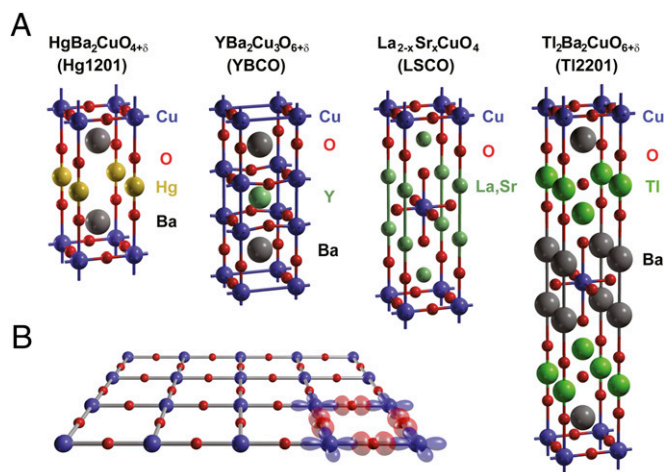
Fig. 1. Crystal structures of four cuprates. (*A*) The unit cells (total number of atoms, individual versus pairs of CuO$_2$ sheets, *c*-axis dimensions, etc.), most prevalent disorder types, and structural symmetry of these four cuprates differ considerably (for details, see ref. 4 and *SI Appendix*, section 2). For Hg1201, YBCO, and Tl2201, the hole concentration in the CuO$_2$ sheets is altered by varying the density of interstitial oxygen atoms (each interstitial oxygen introduces up to two holes into nearby CuO$_2$ sheets), whereas in LSCO holes are introduced by replacing La^{3+} with Sr^{2+} (p = x in this case). Hg1201 has a particularly simple crystal structure. It is the first member of the Ruddlesden–Popper family HgBa$_2$CuCa$_{n-1}$Cu$_n$O$_{2n+2+\delta}$, features one CuO$_2$ sheet per formula unit (*n* = 1), and the highest optimal T_c (T_c^{max} = 98 K) of all such single-layer compounds [e.g., T_c^{max} = 39 K and 93 K for LSCO and Tl2201, respectively (4)]. Furthermore, the physical properties of Hg1201 appear to be least affected by disorder (e.g., the residual resistivity is negligible; Figs. 2 and 3). (*B*) The universal building block of the high-T_c cuprates is the CuO$_2$ sheet. The most important electronic orbitals, Cu $d_{x^2-y^2}$ and O p_σ, are shown.

which disorder effects are known to be significant (4), or for other cuprates in the doping range 0.11 < p < 0.30. However, as summarized in Fig. 3, a quadratic planar resistivity has been observed in a few cases: underdoped YBCO (p = 0.03 and 0.09) (8, 10, 11), underdoped LSCO (p = 0.02 and 0.08) (8), as well as strongly overdoped LSCO (p = 0.33). The latter has been argued to be a Fermi liquid (16). In Fig. 3*E* and *SI Appendix*, section 5, we demonstrate that $\rho \propto T^2$ also holds at intermediate temperatures for prior data for LSCO at p = 0.01 (9). Tl2201 (13) (T_c = 15 K; Fig. 3*I*) and LSCO (14) at $p \approx 0.30$ are in close proximity to the putative Fermi liquid regime, and the description of the planar resistivity requires only a small additional *T*-linear component. For underdoped YBCO at $p \approx 0.11$ in a 55 T magnetic field, an approximately quadratic resistive behavior was reported down to very low temperature (12).

In Fig. 4*B* and *SI Appendix*, section 6, we demonstrate that the four characteristic temperatures and the underlying (hidden) quadratic resistive regimes of YBCO, LSCO, and Bi2201 can be identified consistently from prior contour plots of the second temperature derivative of the resistivity (20). Hg1201 and YBCO are structurally very different cuprates, with one and two CuO$_2$ sheets per unit cell, respectively (Fig. 1). However, as shown in Fig. 4, the doping-dependent temperatures T^*, T^{**}, T', and T_c determined from resistivity, which demarcate five distinct physical regions, are very similar. For both compounds, the opening of the pseudogap at T^* has been shown to be associated with a phase transition to a novel magnetically ordered state (21). The onset of the $\rho \propto T^2$ behavior below T^{**} agrees surprisingly well with characteristic temperatures determined by two other probes: the maximum of the thermoelectric power (TEP) for both Hg1201 (22) and YBCO (23, 24) (*SI Appendix*, section 1), and the onset of a Kerr rotation signal for YBCO (25). In both

compounds, superconducting fluctuations affect the dc conductivity only near T_c (below T').

Universal Sheet Resistance. We now analyze the doping dependences of the linear and quadratic contributions to the sheet resistance for Hg1201, YBCO (7, 8, 10–12), Tl2201 (13, 17), and LSCO (8, 9, 13–15). As shown in Figs. 4 and 5, four primary regions need to be distinguished: the *T*-linear regime (p < $p^* \approx$ 0.19 and $T > T^*$), the two seemingly disconnected quadratic regimes (p < p^* and $T < T^{**}$; p > 0.30 and $T < 55$ K), and the intermediate "mixed" region ($p^* <$ p < 0.30) accessed in high magnetic fields [data mostly for LSCO (14)].

For several reasons, the results in Figs. 2 and 5 are remarkable. First, for underdoped Hg1201, we observe a clear and dramatic "switch" of scattering mechanisms upon cooling: there is no discernible quadratic (linear) contribution above T^* (between T^{**} and T') and the residual resistivity is tiny. Second, $A_{1\square}$ and $A_{2\square}$ are universal, despite substantial differences in crystal structure, disorder, and optimal T_c of the four compounds (4). Consequently, the states near the Fermi level that contribute to the planar transport are essentially identical, and the underlying fundamental planar resistivity in the normal state of the cuprates is now known. Third, $A_{1\square}$ (for p < p^*) and $A_{2\square}$ (except near p^*) are, to a good approximation, simply proportional to the inverse hole concentration. Fourth, the scattering mechanism responsible for the linear temperature dependence of the resistivity is clearly related to fluctuations that disappear upon cooling below T^* and doping beyond p^*. This is apparent from the fact that purely *T*-linear behavior is observed only above T^*, and also from the behavior of the resistivity just above p^* (Fig. 5*B*), where $A_{1\square}$ for both LSCO and Tl2201 (13, 14) decreases faster than $1/p$ and approaches zero as superconductivity disappears around p = 0.30.

Discussion and Conclusions

Discussion of Doping Dependence. Based on the prior observation of metallic resistive behavior at low hole concentrations, a real-space picture of mesoscopic phase segregation was proposed, with a doping-dependent change of the effective volume relevant to charge transport (9). However, the evidence for such phase segregation in different cuprate families is varied, which appears difficult to reconcile with our observation of universality over a wide doping range (Fig. 5). Another viewpoint is that much of the cuprate phase diagram is controlled by an underlying quantum critical point (26, 27), which is supported by observations of novel magnetism below T^* (21, 28). In quantum critical-point theories, the effective interactions among electrons, and consequently all single-particle renormalization phenomena are assumed to be controlled by a fluctuating order parameter of some kind. Scattering off such fluctuations for $T > T^*$ is proposed to cause the linear-T dependence of the resistivity. Interpreted in this fashion, the result in Fig. 5 indicates that the critical fluctuations either condense below T^* (p < p^*) or gradually disappear (p > p^*). We note, though, that the $1/p$ dependence of $A_{1\square}$ and the quadratic resistive behavior for $T < T^{**}$ are not predicted by existing quantum critical-point theories.

A more specific picture is obtained by using the Drude formula $\rho = m^*/(ne^2\tau)$, which only assumes that it is possible to separate the scattering rate ($1/\tau$) from the ratio of the carrier effective mass to density (m^*/n) (29). The observation of distinct power-law behaviors ($\rho_\square = A_{1\square}T$ and $A_{2\square}T^2$) over a wide doping range below p^* suggests that the scattering rate is proportional to T and T^2 in the respective regions of the phase diagram. One interpretation of the result in Fig. 5 is that the doping dependences of the scattering rates and carrier densities in the Drude expression compensate exactly in such a way that $A_{1\square} \propto A_{2\square} \propto 1/p$. However, the simplest interpretation of this proportionality for p < p^* is to associate the doping dependence of the resistivity solely with the doped carriers: $n = p$. It follows that the respective
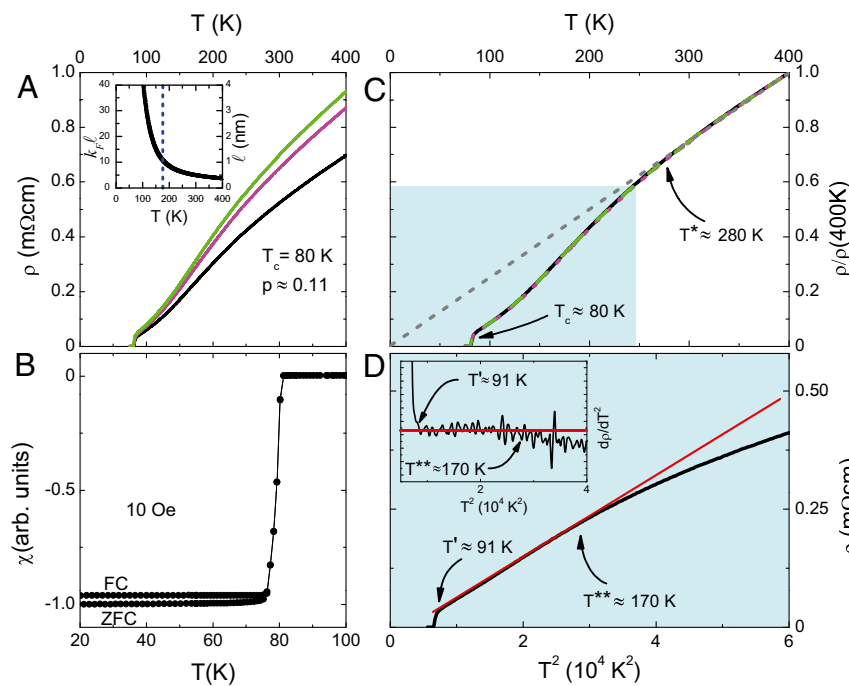
Fig. 2. *ab*-plane dc resistivity and magnetic susceptibility for underdoped Hg1201 ($T_c = 80$ K). (*A*) Resistivity as a function of temperature for three samples. Because the samples are cleaved, their shapes are irregular, and consequently the absolute value of the resistivity ($\rho \approx 0.6$ mΩ·cm at 300 K) could only be determined with about 20% accuracy (see *SI Appendix*, section 4, for experimental methods and detailed results for other hole concentrations). (*Inset*) Estimates of mean free path, l, and $k_F l$ (*SI Appendix*, section 10). The blue vertical dashed line indicates T^{**}. (*B*) Magnetic susceptibility [zero–field-cooled (ZFC) and field-cooled (FC)] for one of the samples after its preparation for resistivity measurements (*SI Appendix*, section 4) reveals a sharp onset T_c of 80 K. The FC/ZFC ratio of 97% is exceptionally large, indicative of very high sample quality (19). (*C*) When normalized at 400 K, the data in *A* collapse onto a single curve, indicating high bulk homogeneity. High-temperature linear behavior: $\rho = \rho_0 + A_1 T$ (dashed line), with $\rho_0 \approx 0$ and $T^* \approx 280$ K. (*D*) The resistivity exhibits a quadratic temperature dependence between $T' \approx 90$ K and $T^{**} \approx 170$ K. This is also seen from the plot of $d\rho/d(T^2)$ (*Inset*). The red lines are guides to the eye. The horizontal and vertical ranges correspond to the blue area in *C*.

scattering rates τ_1 and τ_2 as well as the effective mass m^* are doping independent and universal. This interpretation is consistent with several experimental observations (9, 30–32), e.g., that the Fermi arc length in the pseudogap regime is proportional to p (31, 33) and that the optical effective mass enhancement is doping independent, whereas the effective optical charge density varies almost linearly with doping (32).

Furthermore, because $A_{1\square} \propto A_{2\square} \propto 1/p$ for p < p^*, the effective number of carriers would seem to remain unaffected by the closing of the pseudogap with increasing temperature. The dominant contribution to the conductivity at all temperatures might therefore come from the relatively fast carriers in the nodal regions (34, 35). Alternatively, to explain the nodal character of the cuprates, one might invoke either the scattering off magnetic fluctuations (hot spots) associated with the antinodes or electronic scattering involving van Hove singularities near the Fermi surface (36). Finally, the antinodal states might be at the Planckian dissipation limit (14) beyond which coherent single-particle propagation is inhibited (37, 38). It has been argued that the pseudogap formation may then be viewed as the lowering of the electronic energy in response to this intense scattering, preventing the scattering from remnant quasiparticle states into the "hot" antinodal regions (14).

It is instructive to extend the above interpretation based on the Drude formula to the overdoped regime. For p > p^*, the cuprates feature a large Fermi surface volume, which in accordance with Luttinger's theorem corresponds to $1 + p$ rather than p carriers (39, 40). For hole concentrations between p^* and $p \approx 0.30$, the planar resistivity of overdoped LSCO and Tl2201 exhibits both linear and quadratic contributions below ≈200 K in a high *c*-axis magnetic field that suppresses the superconductivity (13, 14). We note that the linear term smoothly connects to the (zero-field) $A_{1\square} \propto 1/p$ behavior for p < p^* and T > T^* (Fig. 5). Above p^*, purely Fermi liquid-like quadratic resistivity has been observed for LSCO at p = x = 0.33, the highest doping level attained in bulk crystals (16) (*SI Appendix*, section 7). Unlike $A_{1\square}$, the determination of $A_{2\square}$ near p^* is ambiguous, as it depends on the choice of polynomial or parallel resistor fit (14). However, above $p \approx 0.26$, the contribution of the linear term is small, and the simple relation $A_{2\square} \propto 1/p$ appears to hold again. This

suggests that the scattering mechanism in the pseudogap regime might be the same as in the putative Fermi-liquid state at high doping.

The clarification of the nodal/antinodal dichotomy, which may require the explicit theoretical treatment of oxygen degrees of freedom (38) (*SI Appendix*, section 8), appears to be essential to understand this observation.

Pseudogap Phenomenon vs. Fermi Liquid. The underdoped cuprates have been suggested to be "nodal metals" described by a two-component optical conductivity, with a low-energy Drude component associated with coherent quasiparticles on the Fermi arcs observed in photoemission experiments (10, 30). Photoemission experiments also indicate a nearly material and doping-independent near-nodal band structure characterized by a sizable Fermi velocity on the arcs (34, 35). Furthermore, the in-plane infrared spectral weight is found to be insensitive to the opening of the pseudogap (41). These results are consistent with our observations.

The quadratic resistive behavior in the pseudogap regime extends to rather high temperatures (Fig. 3 and *SI Appendix*, section 9) and is cut off at low temperature by either (non-universal) charge localization effects (9, 11) or superconducting fluctuations. We emphasize that an approximately quadratic temperature dependence was also reported for YBCO ($p \approx 0.11$) down to low temperature (about 4 K) (Fig. 4*B*) after the suppression of superconductivity by a high magnetic field (12), and that the corresponding value of $A_{2\square}$ falls on the universal plots of Fig. 5 *E* and *F*. As shown in Fig. 2*A*, for Hg1201 at temperatures below T^{**}, the mean-free path is considerably larger than the planar lattice constant; thus, the Ioffe–Regel criterion (42) for a good metal is satisfied (*SI Appendix*, section 10). The observation for YBCO of quantum oscillations in high magnetic fields appears to provide additional support for a Fermi-liquid state in the underdoped cuprates (43), although this phenomenon occurs in a rather narrow doping range, is suggestive of small (electron) pockets, and has not yet been shown to be universal. Additional evidence for seemingly conventional metallic behavior comes from the well-known T^2 dependence of the Hall angle (*SI Appendix*, section 6) (8). Furthermore, motivated by the present work, optical conductivity measurements of Hg1201 indeed have revealed
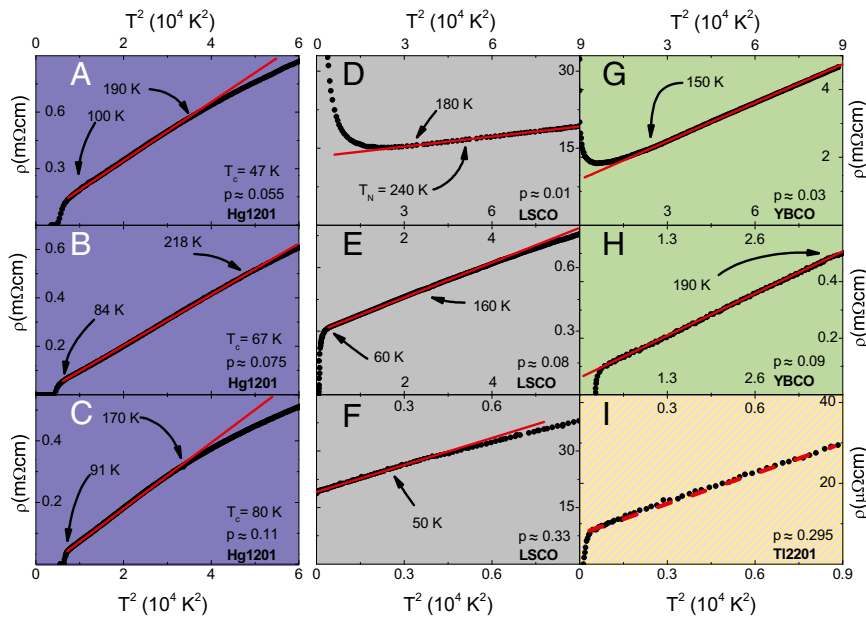
Fig. 3. Doping and compound dependence of T^2 resistivity. (*A–C*) Quadratic resistivity in underdoped Hg1201 at three doping levels, observed from $T' \approx T_c + 15$ K (above the "superconducting tail" for samples with $T_c = 47$ K; *SI Appendix*, section 4) up to T^{**}. (*D*) Similar behavior for LSCO is demonstrated for prior data at p = 0.01 (*SI Appendix*, section 5), where the quadratic behavior persists into the Néel state ($T_N = 240$ K) (9). For LSCO, $\rho \propto T^2$ was previously reported (8) for p = 0.02 (not shown), (*E*) p = 0.08, and (*F*) p = 0.33 (16). For YBCO in zero magnetic field, it was reported for (*G*) p = 0.03 (8) and (*H*) p = 0.09 (10). (*I*) For Tl2201 at p = 0.295, the resistivity increases more slowly than T^2 (black dotted curve is slightly concave with respect to the straight dashed red line), which implies the presence of a small linear contribution (13). The red lines are guides to the eye. Lower (T_ρ') and upper (T_ρ^{**}) temperatures at which resistivity begins to deviate from the quadratic behavior are indicated by arrows. (See *SI Appendix*, sections 4 and 6, for estimates of characteristic temperatures and hole concentrations, respectively.)

the quadratic frequency dependence and the temperature–frequency scaling expected for a Fermi liquid (44). Nevertheless, the situation is highly unconventional, as exemplified by the presence of arcs and by the evidence for a quantum critical point. Interestingly, NMR results for LSCO and Hg1201 imply a two-component local magnetic susceptibility in the pseudogap regime, one temperature-independent above T_c, i.e., Fermi-liquid-like, and the other temperature-dependent and correlated

with the formation of the pseudogap (45). Further evidence for a two-component quasiparticle spectrum for p < p^* comes from a recent analysis of the electronic entropy in several cuprates (46).

Updated Phase Diagram. Fig. 6 shows the updated phase diagram of the cuprates. Fig. 6*A* focuses on the nonsuperconducting properties, neglecting complications (Fig. 6*B*) related to low
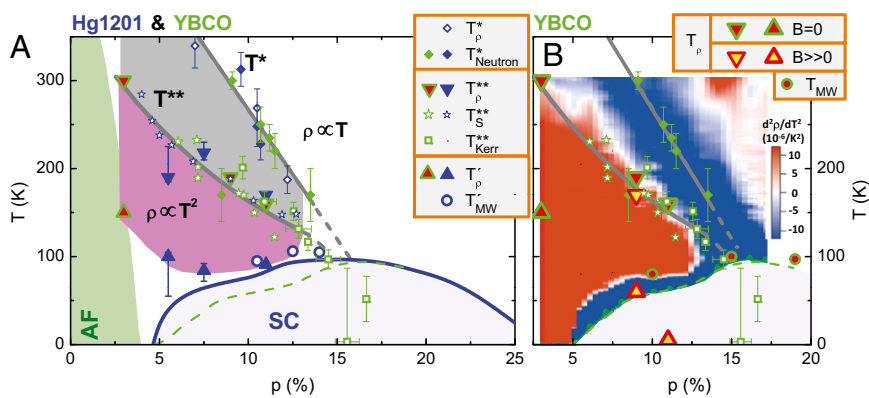

Fig. 4. Phase diagram of Hg1201 and YBCO. (*A*) Pseudogap temperature T^*, determined from deviation from linear-T resistivity (T^*_ρ) and neutron-scattering (21, 28) experiments ($T^*_{Neutron}$). The gray shaded area indicates the crossover to the quadratic regime (magenta) found below T^{**}. The latter ends with the measurable appearance of SC fluctuations at T', in agreement with microwave (T_{MW}) measurements for Hg1201 (49) and YBCO (50), or when localization effects set in (around 150 K for YBCO at p = 0.03) (8). The temperatures of the TEP peak (T_S^{**}) [extracted from published data for underdoped Hg1201 (22) and for YBCO (23, 24)] and of the onset of the Kerr effect (T_{Kerr}^{**}) for YBCO (25) track T^{**}_ρ from dc resistivity. The blue and green symbols correspond to Hg1201 and YBCO, respectively. The green dashed line corresponds to the $T_c(p)$ of YBCO. The blue line is obtained from available data for $T_c(p)$ of Hg1201 (up to p = 0.21) (22) and extended to higher doping (*SI Appendix*, section 6). The gray lines for $T^*(p)$ and $T^{**}(p)$ are guides to the eye. Antiferromagnetic (AF) phase is schematically indicated by the green shaded area. (*B*) The underlying T^2 (red contour) regime of YBCO is effectively captured by a map of the resistivity curvature (20). Quadratic resistive behavior is also apparent after applying a high c-axis magnetic field of about 50 T (11, 12). For p = 0.11 (12), it was reported that the field was sufficiently high to suppress the superconductivity and reveal approximately quadratic resistive behavior to low temperature. See *SI Appendix*, section 6, for estimates of hole concentrations.
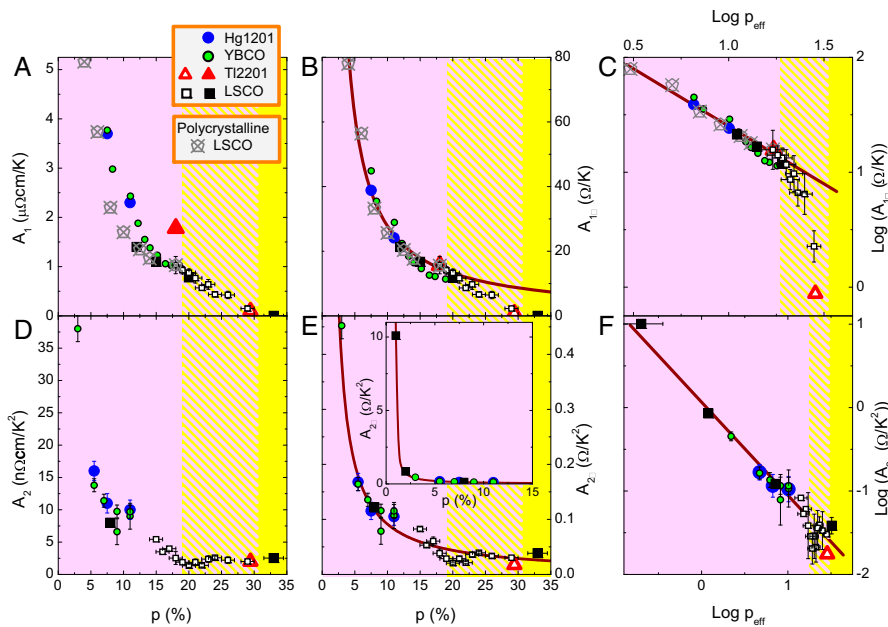
Fig. 5. Doping dependence of coefficients A_1, $A_{1\square}$, A_2, and $A_{2\square}$. There exist four distinct regimes: for $p < 0.19$ (pink) either (i) $\rho \propto A_1 T$ ($T > T^*$) or (ii) $\rho \propto A_2 T^2$ ($T^{**} > T > T'$) is observed (filled symbols); (iii) for $0.19 \leq p \leq 0.3$ (pink/yellow hatched area), the resistivity [for LSCO (14) and Tl2201 (13); LSCO data obtained in a high magnetic field] does not exhibit pure power-law behavior, and prior results from fits to $1/\rho = 1/(\rho_0 + A_1 T + A_2 T^2) + 1/\rho_{max}$, rather than $\rho = \rho_0 + A_1 T + A_2 T^2$, are shown (open symbols); the two forms were found to give closely similar results for A_1 at all measured hole concentrations, and for A_2 above $p = 0.26$ (14). The latter form yields a lower estimate of $A_2 \approx 0$ near p^*; (iv) putative Fermi-liquid regime for $p > 0.3$ (below about 50 K) (yellow). (A and D) A_1 and A_2 versus hole concentration p. (B and E) Demonstration of universal behavior of $A_{1\square}(p)$ and $A_{2\square}(p)$, with approximately constant ratio $A_{1\square}/A_{2\square} \approx 325$ K for $p < 0.19$. Brown lines indicate simple $1/p$ power-law behavior. (C and F) Log–log plots. A somewhat better linear fit (brown line) is obtained with effective hole concentrations, $A_{1\square}(p_{eff}) \propto 1/(p - p_1)$ (for $0.04 \leq p \leq 0.19$) and $A_{2\square}(p_{eff}) \propto 1/(p - p_2)$ ($0.01 \leq p \leq 0.33$), with nonzero $p_1 = p_2 = 0.007(2)$. For LSCO, data for polycrystalline samples (15) are rescaled by factor of 1/5.5 to match single crystal data. See *SI Appendix*, section 6, for estimates of hole concentrations.

structural symmetry, disorder and localization effects (4, 9, 11), the "stripe" instability near $p \approx 1/8$ (47), and inhomogeneities near p^* (14). The pseudogap temperature T^* has been associated with a transition to a state with novel magnetic order in both YBCO and Hg1201 (21). The coincidence of T^{**} with the onset of the polar Kerr effect in YBCO (25) raises the possibility that this temperature may be universally associated with a second phase transition above T_c. There exist at least two qualitatively different scenarios near p^* that cannot yet be distinguished. Either both $T^*(p)$ and $T^{**}(p)$ approach zero at $p^* \approx 0.2$, the

putative quantum critical point, or the two characteristic temperatures cross near optimal doping. A possible caveat is that, even if much of the phase diagram is controlled by a quantum critical point, this point may be inaccessible through the variation of physical parameters such as doping and magnetic field. Even though the Fermi surface undergoes a change in topology as it breaks up into arcs on the underdoped side of the phase diagram, the electronic scattering mechanism that gives rise to the quadratic resistive behavior appears to be the same at the extreme doping levels of 1% and 33%. In the quadratic resistive
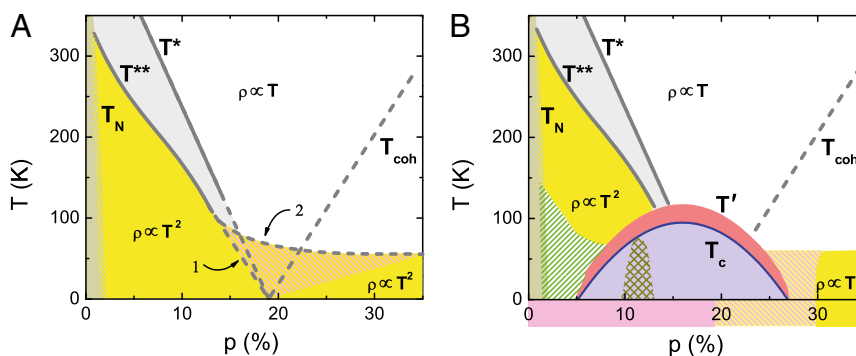
Fig. 6. Modified phase diagram of the cuprates. (A) Underlying phase diagram in the absence of disorder and superconductivity. The undoped parent compounds are Mott (charge transfer) insulators. Antiferromagnetic (AF) order below T_N extends to nonzero doping. Quadratic resistive behavior (observed in LSCO even at $p = 0.01$, for $T > 150$ K) extends into the AF region. The ground state may be insulating up to a small, nonzero hole concentration. $T^*(p)$, and possibly also $T^{**}(p)$, mark phase transitions. T_{coh} corresponds to the loss of antinodal quasiparticle coherence, as observed in photoemission experiments (13). Two scenarios for $T^{**}(p)$ are indicated by arrows: $T^{**}(p)$ either approaches zero at the putative quantum critical point at $p^* \approx 0.19$ or crosses $T^*(p)$ (hatched area). The putative quantum critical point may be inaccessible experimentally (see main text). (B) Phase diagram with disorder, superconductivity and "1/8" anomaly. Superconducting phase (purple); doping/temperature range of the superconducting fluctuations (49, 50): red; localization effects (11): green; $p = 1/8$ anomaly (47): olive; possible chemical inhomogeneities (14) (for LSCO) immediately above p^*: orange. The three regimes from Fig. 5 are marked along the horizontal axis by corresponding colors.

regime, the underdoped cuprates are rather good metals and may need to be thought of as a two-component electron fluid, as a result of correlations associated with the formation of the pseudogap state, in which the metallic component evolves from the Fermi liquid at the highest doping. A $\rho \propto T^2$ behavior was also found on the electron-doped side of the phase diagram. However, in contrast to our findings for the hole-doped cuprates, superconductivity appears to evolve from a state that exhibits T-linear resistivity (48) (*SI Appendix*, section 6).

The present work demonstrates that the quadratic planar resistivity is a universal property of the underdoped cuprates, and that the structurally simple model compound Hg1201 exhibits negligible residual resistivity and a dramatic switch from T-linear to quadratic behavior upon cooling. Although the resistivity is generally highly sensitive to compound-specific characteristics, we have furthermore achieved a quantitative, universal understanding of both the linear and quadratic regimes by considering the resistance per principal building block, the copper–oxygen sheet, of four structurally distinct cuprates. Analysis of compound-specific deviations (e.g., for Bi2201 and Bi2212, or for LSCO near $p = 0.12$) from the underlying behavior reported here can be expected to lead to new insights into the nonuniversal features exhibited by individual compounds. Most importantly, the present work provides a quantitative basis for the development of a comprehensive theoretical understanding of these fascinating materials.

1. Ashcroft NW, Mermin ND (1976) *Solid State Physics* (Holt, Rinehart and Winston, New York).
2. Laughlin RB (1981) Quantized Hall conductivity in two dimensions. *Phys Rev B* 23(10): 5632–5633.
3. Anderson PW (1987) The resonating valence bond state in La_2CuO_4 and superconductivity. *Science* 235(4793):1196–1198.
4. Eisaki H, et al. (2004) Effect of chemical inhomogeneity in bismuth-based copper oxide superconductors. *Phys Rev B* 69(6):064512-1–064512-8.
5. Alloul H, Ohno T, Mendels P (1989) ^{89}Y NMR evidence for a Fermi-liquid behavior in $YBa_2Cu_3O_{6+x}$. *Phys Rev Lett* 63(16):1700–1703.
6. Timusk T, Statt B (1999) The pseudogap in high-temperature superconductors: An experimental survey. *Rep Prog Phys* 62(1):61–122.
7. Ito T, Takenaka K, Uchida S (1993) Systematic deviation from T-linear behavior in the in-plane resistivity of $YBa_2Cu_3O_{7-y}$: Evidence for dominant spin scattering. *Phys Rev Lett* 70(25):3995–3998.
8. Ando Y, Kurita Y, Komiya S, Ono S, Segawa K (2004) Evolution of the Hall coefficient and the peculiar electronic structure of the cuprate superconductors. *Phys Rev Lett* 92(19):197001-1–197001-4.
9. Ando Y, Lavrov AN, Komiya S, Segawa K, Sun XF (2001) Mobility of the doped holes and the antiferromagnetic correlations in underdoped high-T_c cuprates. *Phys Rev Lett* 87(1):017001-1–017001-4.
10. Lee YS, et al. (2005) Electrodynamics of the nodal metal state in weakly doped high-T_c cuprates. *Phys Rev B* 72(5):054529-1–054529-13.
11. Rullier-Albenque F, Alloul H, Balakirev F, Proust C (2008) Disorder, metal-insulator crossover and phase diagram in high-T_c cuprates. *Europhys Lett* 81(3):37008-1–37008-6.
12. LeBoeuf D, et al. (2011) Lifshitz critical point in the cuprate superconductor $YBa_2Cu_3O_y$ from high-field Hall effect measurements. *Phys Rev B* 84(1):014507-1–014507-7.
13. Hussey NE (2011) What drives pseudogap physics in high-T_c cuprates? A view from the (resistance) bridge. *J Phys Chem Solids* 72(5):529–532.
14. Cooper RA, et al. (2009) Anomalous criticality in the electrical resistivity of $La_{2-x}Sr_xCuO_4$. *Science* 323(5914):603–607.
15. Nakano T, et al. (1994) Magnetic properties and electronic conduction of superconducting $La_{2-x}Sr_xCuO_4$. *Phys Rev B Condens Matter* 49(22):16000–16008.
16. Nakamae S, et al. (2009) Erratum: Electronic ground state of heavily overdoped nonsuperconducting $La_{2-x}Sr_xCuO_4$. *Phys Rev B* 79(21):219904–1.
17. Ma YC, Wang NL (2006) Infrared scattering rate of overdoped $Tl_2Ba_2CuO_{6+\delta}$. *Phys Rev B* 73(14):144503-1–144503-7.
18. Zhao X, et al. (2006) Crystal growth and characterization of the model high-temperature superconductor $HgBa_2CuO_{4+\delta}$. *Adv Mater* 18(24):3243–3247.
19. Barišić N, et al. (2008) Demonstrating the model nature of the high-temperature superconductor $HgBa_2CuO_{4+\delta}$. *Phys Rev B* 78(5):054518-1–054518-7.
20. Ando Y, Komiya S, Segawa K, Ono S, Kurita Y (2004) Electronic phase diagram of high-T_c cuprate superconductors from a mapping of the in-plane resistivity curvature. *Phys Rev Lett* 93(26):267001-1–267001-4.
21. Li Y, et al. (2008) Unusual magnetic order in the pseudogap region of the superconductor $HgBa_2CuO_{4+\delta}$. *Nature* 455(7211):372–375.
22. Yamamoto A, Hu W, Tajima S (2000) Thermoelectric power and resistivity of $HgBa_2CuO_{4+\delta}$ over a wide doping range. *Phys Rev B* 63(2):024504-1–024504-6.
23. Cooper JR, Loram JW (1996) Some correlations between the thermodynamic and transport properties of high-T_c oxides in the normal state. *J Physique I* 6(12):2237–2263.
24. Cooper JR, Obertelli SD, Carrington A, Loram JW (1991) Effect of oxygen depletion on the transport properties of $YBa_2Cu_3O_{7-\delta}$. *Phys Rev B Condens Matter* 44(21):12086–12089.
25. Kapitulnik A, Xia J, Schemm E, Palevski A (2009) Polar Kerr effect as probe for time-reversal symmetry breaking in unconventional superconductors. *New J Phys* 11:055060-1–055060-18.
26. Varma CM (1999) Pseudogap phase and the quantum-critical point in copper-oxide metals. *Phys Rev Lett* 83(17):3538–3541.
27. Laughlin RB, Lonzarich GG, Monthoux P, Pines D (2001) The quantum criticality conundrum. *Adv Phys* 50(4):361–365.
28. Li Y, et al. (2010) Hidden magnetic excitation in the pseudogap phase of a high-T(c) superconductor. *Nature* 468(7321):283–285.
29. Gor'kov LP, Teitel'baum GB (2008) Mobility and its temperature dependence in underdoped $La_{2-x}Sr_xCuO_4$ interpreted as viscous motion of charges. *Phys Rev B* 77(18): 180511(R)-1–180511-4.
30. Basov DN, Timusk T (2005) Electrodynamics of high-T_c superconductors. *Rev Mod Phys* 77(2):721–779.
31. Yoshida T, Hashimoto M, Vishik IM, Shen Z-X, Fujimori A (2012) Pseudogap, superconducting gap, and Fermi arc in high-T_c cuprates revealed by angle-resolved photoemission spectroscopy. *J Phys Soc Jpn* 81(6):011006-1–011006-10.
32. Dai YM, et al. (2012) Doping evolution of the optical scattering rate and effective mass of $Bi_2Sr_{2-x}La_xCuO_6$. *Phys Rev B* 85(9):092504-1–092504-4.
33. Lee PA, Wen X-G (1997) Unusual superconducting state of underdoped cuprates. *Phys Rev Lett* 78(21):4111–4114.
34. Zhou XJ, et al. (2003) High-temperature superconductors: Universal nodal Fermi velocity. *Nature* 423(6938):398.
35. Hashimoto M, et al. (2008) Doping evolution of the electronic structure in the single-layer cuprate $Bi_2Sr_{2-x}La_xCuO_{6+\delta}$: Comparison with other single-layer cuprates. *Phys Rev B* 77(9):094516-1–094516-9.
36. Hlubina R, Rice TM (1995) Resistivity as a function of temperature for models with hot spots on the Fermi surface. *Phys Rev B Condens Matter* 51(14):9253–9260.
37. Zaanen J (2004) Superconductivity: Why the temperature is high. *Nature* 430(6999): 512–513.
38. Barišić S, Barišić OS (2012) Approaching large U_d high-T_c cuprates from the covalent side. *J Supercond Nov Magn* 25(3):669–676.
39. Platé M, et al. (2005) Fermi surface and quasiparticle excitations of overdoped $Tl_2Ba_2CuO_{6+\delta}$. *Phys Rev Lett* 95(7):077001-1–077001-4.
40. Hussey NE, Abdel-Jawad M, Carrington A, Mackenzie AP, Balicas L (2003) A coherent three-dimensional Fermi surface in a high-transition-temperature superconductor. *Nature* 425(6960):814–817.
41. Santander-Syro AF, et al. (2001) Absence of a loss of in-plane infrared spectral weight in the pseudogap regime of $Bi_2Sr_2CaCu_2O_{8-\delta}$. *Phys Rev Lett* 88(9):097005-1–097005-4.
42. Ioffe AF, Regel AR (1960) Noncrystalline, amorphous and liquid electronic semiconductors. *Prog Semicond* 4:237–291.
43. LeBoeuf D, et al. (2007) Electron pockets in the Fermi surface of hole-doped high-T_c superconductors. *Nature* 450(7169):533–536.
44. Mirzaei SI, et al. (2013) Spectroscopic evidence for Fermi liquid-like energy and temperature dependence of the relaxation rate in the pseudogap phase of the cuprates. *Proc Natl Acad Sci USA* 110(15):5774–5778.
45. Haase J, et al. (2012) Two-component uniform spin susceptibility of superconducting $HgBa_2CuO_{4+\delta}$ single crystals measured using ^{63}Cu and ^{199}Hg nuclear magnetic resonance. *Phys Rev B* 85(10):104517-1–104517-6.
46. Storey JG, Tallon JL (2012) Two-component electron fluid in underdoped high-T_c cuprate superconductors. *Europhys Lett* 98(1):17011-1–17011-5.
47. Kivelson SA, et al. (2003) How to detect fluctuating stripes in the high-temperature superconductors. *Rev Mod Phys* 75(4):1201–1241.
48. Butch NP, Jin K, Kirshenbaum K, Greene RL, Paglione J (2012) Quantum critical scaling at the edge of Fermi liquid stability in a cuprate superconductor. *Proc Natl Acad Sci USA* 109(22):8440–8444.
49. Grbić MS, et al. (2009) Microwave measurements of the in-plane and c-axis conductivity in $HgBa_2CuO_{4+\delta}$: Discriminating between superconducting fluctuations and pseudogap effects. *Phys Rev B* 80(9):094511-1–094511-5.
50. Grbić MS, et al. (2011) Temperature range of superconducting fluctuations above T_c in $YBa_2Cu_3O_{7-\delta}$ single crystals. *Phys Rev B* 83(14):144508-1–144508-12.